JOURNAL OF SPACECRAFT AND ROCKETS
Vol. 51, No. 3, May–June 2014

Supersonic Retropropulsion Computational-Fluid-Dynamics Validation with Ames 9 × 7 Foot Test Data

Daniel Guy Schauerhamer*
NASA Johnson Space Center, Houston, Texas 77058
Kerry A. Zarchi†
NASA Ames Research Center, Moffett Field, California 94035
and
William L. Kleb‡ and Karl T. Edquist§
NASA Langley Research Center, Hampton, Virginia 23681

DOI: 10.2514/1.A32694

A validation study of computational fluid dynamics for supersonic retropropulsion was conducted using three Navier–Stokes flow solvers. The study compared results from the computational-fluid-dynamics codes to each other and to wind-tunnel test data obtained in the NASA Ames Research Center 9 × 7 ft Unitary Plan Wind Tunnel. Comparisons include surface pressure coefficient as well as unsteady plume effects and cover a range of Mach numbers, levels of thrust, and angles of orientation for zero-, one-, three-, and four-nozzle configurations. Flow-structure behavior changed with thrust and angle of orientation for all nozzle configurations. In general, the solvers compared best with the test data for the steadier cases of the one-nozzle and high-thrust three-nozzle configurations. Deviation in surface pressure was noted for the more unsteady cases and near transitions in behavioral modes. Strengths and weaknesses of the solvers are identified, and possible error sources are discussed.

Nomenclature

A_{ref}	=	19.63 in.^{2}, reference area
$C_{A,\text{aero}}$	=	aerodynamic contribution to axial force coefficient
$C_{A,\text{total}}$	=	$C_T + C_{A,\text{aero}}$, total axial force coefficient
C_P	=	pressure coefficient
C_T	=	$T/(\bar{q}A_{\text{ref}})$, thrust coefficient
L	=	10.5 in., model length
$P_{o,\text{jet}}$	=	jet total pressure, psia
$\bar{q}$	=	dynamic pressure, psia
R	=	2.5 in., model radius
Re	=	Reynolds number
r	=	radial coordinate, in.
T	=	thrust, lbf
$T_{o,\text{jet}}$	=	jet total temperature, °R
x	=	axial coordinate, in
α	=	angle of attack, deg
θ	=	model cylindrical angle, deg
ϕ	=	roll angle, deg

I. Introduction

SUPERSONIC retropropulsion (SRP) is a potentially viable means to decelerate high-mass vehicles entering the Martian atmosphere [1–6]. Previous methods of supersonic deceleration, including parachutes and heat shields, are not scalable for exploration-type vehicles, which can potentially weigh tens of metric tons. Because ground and flight testing of SRP at entry conditions can be difficult and cost-prohibitive, the development of this enabling technology can be enhanced with the ability to predict the flowfield numerically using computational fluid dynamics (CFD).

SRP results in a complex flow structure involving shocks, shear layers, recirculation, and stagnation regions, which makes validation of the CFD methods a high priority. The validation process includes using multiple CFD codes to compare to historical and recent wind-tunnel tests. Three CFD codes are being applied to SRP: Data Parallel Line Relaxation (DPLR) [7], Fully Unstructured Navier–Stokes Three-Dimensional (FUN3D) [8,9], and OVERset grid FLOW solver (OVERFLOW) [10]. The codes all solve the Navier–Stokes equations but differ in implementation, grid type, and numerical methods. Through code-to-code and code-to-test comparisons, the validity of CFD methods is increased as best practices in grid generation, numerical method selection, and solution advancement are established. With that validity, confidence is built for using CFD to predict those same physics at Mars entry conditions.

CFD validation efforts for SRP were conducted under the NASA Exploration Technology Development Program. The CFD solvers were applied to a historical and a more recent wind-tunnel test [11–13]. Although much was learned through the exercise, the test reports lacked key information for CFD validation. A wind-tunnel test was then conducted for the purpose of CFD validation in the NASA Langley Research Center supersonic 4 × 4 ft Unitary Plan Wind Tunnel (LRC UPWT), the design of which was aided by CFD [14,15]. Through results from the test, CFD best practices were established [16], and an extensive comparison study was conducted [17]. The study yielded promising results, but not all conditions were properly and consistently predicted between the CFD codes. To further the validation exercise, and to obtain higher and more flight-relevant thrust levels, the same model was tested in the NASA Ames Research Center 9 × 7 ft Unitary Plan Wind Tunnel (ARC UPWT). This paper will focus on the subsequent CFD validation study.

Qualitative comparisons of the flow structure will be made by comparing CFD to high-speed shadowgraph images, and quantitative comparisons will be made by comparing time-averaged surface pressure with pressure-tap data from the tunnel. Time-accurate CFD simulations were conducted to capture the inherent unsteadiness of the flowfields. High-frequency pressure-transducer data are also available and have been studied more thoroughly for the LRC UPWT

Presented as Paper 2012-2705 at the 42nd AIAA Fluid Dynamics Conference and Exhibit, New Orleans, LA, 25–28 June 2012; received 24 April 2013; revision received 9 October 2013; accepted for publication 13 November 2013; published online 2 April 2014.

*Aerospace Engineer, Applied Aeroscience and CFD Branch, Jacobs Technology, EG3. Member AIAA.
†Research Scientist, Aerothermodynamics Branch, MS 230-2. Senior Member AIAA.
‡Aerospace Engineer, Aerothermodynamics Branch, MS 408A. Lifetime Member AIAA.
§Aerospace Engineer, Atmospheric flight and Entry Systems Branch, MS 489. Senior Member AIAA.

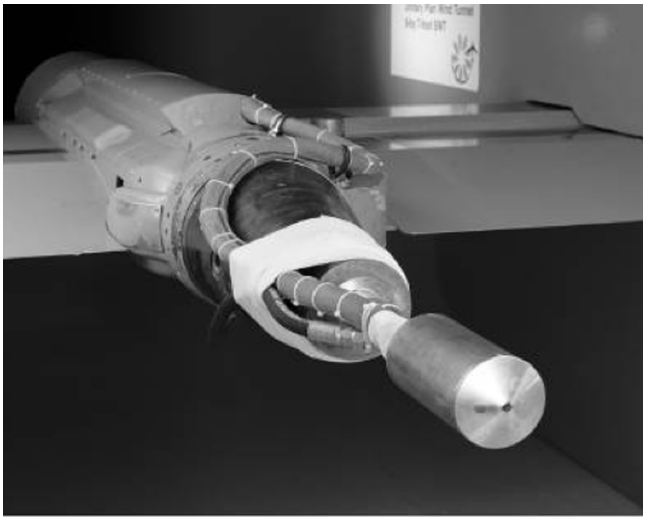

Fig. 1 SRP test model in the one-nozzle configuration in the NASA ARC 9 × 7 ft UPWT.

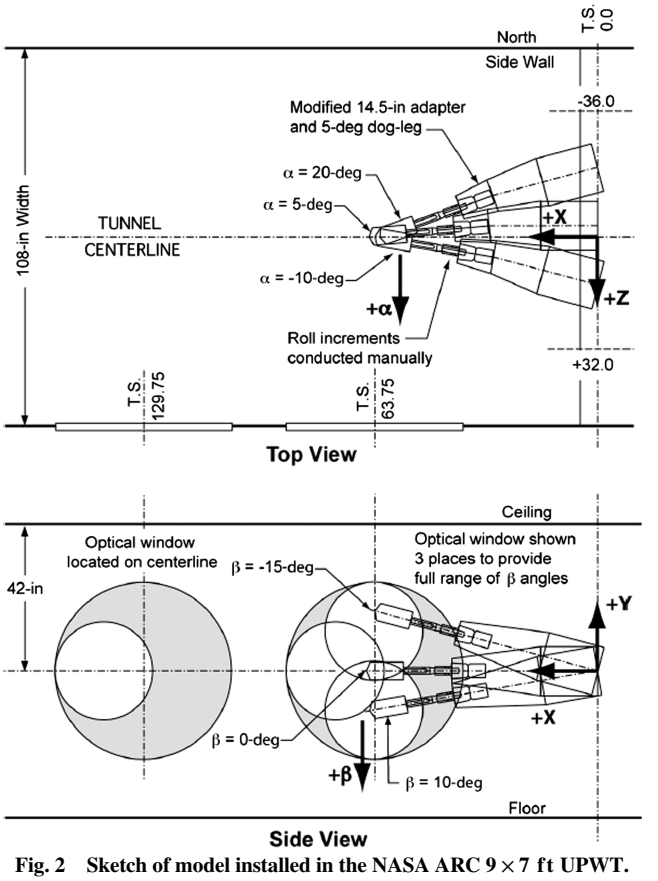

Fig. 2 Sketch of model installed in the NASA ARC 9 × 7 ft UPWT.

test [18] than for the ARC UPWT test. Comparisons of dominant frequencies of certain runs for the LRC UPWT test were discussed in [16]. Neither test used a balance system, and so forces and moments were not measured. However, code-to-code comparisons of forces and moments still contain merit and were conducted for the LRC UPWT test in [17]. For the ARC UPWT test, only a few comparisons of dominant frequencies and forces and moments will be discussed.

An introduction to the SRP flow structure and the CFD solvers is contained in [17]. This paper will introduce the ARC UPWT test, then present results from a sting-sensitivity study, followed by comparisons between codes and the wind-tunnel test (WTT) for the zero-, one-, three-, and four-nozzle configurations. Strengths and weaknesses of the solvers are also discussed.

II. Supersonic Retropropulsion Wind-Tunnel Test

Test 234 in the ARC UPWT was designed specifically for SRP CFD validation and was a follow-on to test 1853 in the LRC UPWT. The motivation for the ARC UPWT test was to use the same model from the previous test in a larger test section to be able to obtain higher and more flight-relevant thrust coefficients ($C_T = T/(\bar{q}A_{\text{ref}})$).

The model consisted of a 70 deg sphere–cone forebody (also referred to as the model face) and a 5-in.-diam cylindrical side body totaling 10.2 in. in length. The model included four nozzles that could be plugged to offer zero-, one-, three-, or four-nozzle configurations. One nozzle was located at the center of the forebody, and the three others were oriented radially every 120 deg at the model's half-radius. Air was used as both the freestream and jet gases. The test data included high-speed shadowgraph movies (5000–10,000 frames per second) and pressure readings from 167 taps including seven 40 kHz pressure transducers. From these data, qualitative comparisons with CFD flow structure and unsteady behavior can be made with the shadowgraph movies as well as averaged surface pressure comparisons with the pressure taps.

The test run matrix included four nozzle configurations: zero, one (center), three (peripheral), and four (center and peripheral). Two Mach numbers were tested: 1.8 and 2.4. The Reynolds number per foot for Mach 1.8 was 1.5 million, and for Mach 2.4, 1.0 and 1.5 million were tested. The total freestream temperature for Mach 1.8 was 550°R and for Mach 2.4 was 555°R. For angles of orientation, α ranged from −8 to 20 deg, and β ranged from 0 to 12 deg. Thrust coefficients ranged from 0 to 10 in increments of 2. To mitigate liquefaction, the jet air supply was heated to 150°F; however, evidence of some liquefaction was noted at high thrust levels. A full description of the test can be found in [19]. Figure 1 is a photograph of the model in the one-nozzle configuration in the test section. Figure 2 is a sketch of the wind-tunnel test section with the model installed and includes the coordinate system [19]. Figure 3 shows diagrams of the model face and side-body pressure-tap layouts [20]. The filled circles represent the high-frequency Kulite® pressure transducers. The figure represents 172 planned pressure taps, including nine 40 kHz pressure transducers; the final count was 167 taps with seven 40 kHz pressure transducers.

Tunnel uncertainty will not be included in this paper because calculations are still underway, but it will be carried out by the same method as the LRC UPWT test [20] as described in [21].

III. Results

The CFD run matrix (Table 1) consisted of 31 cases varying in Mach number, nozzle configuration, thrust coefficient, and angles of orientation. For all Mach numbers tested, the underlying flow physics resembled each other with only minor variations in shock structure. As Mach number increased, the bow shock increased in concavity and decreased in standoff distance from the model face.

All runs in the CFD matrix had a Reynolds number per foot of 1.5 million, with the exception of run 223, which had 1.0 million. For the angles of orientation, most cases vary only in the angle β because the β plane provided better shadowgraph imagery for qualitative comparisons. Runs 279 and 309 included nonzero α angles and were meant to compare total alpha angles α_T of 12 deg at different roll angles ϕ. All cases in the run matrix were computed with OVERFLOW, while a smaller subset was computed with FUN3D and DPLR.

The line plots in this section compare the average surface pressure from the CFD results and the WTT data along $\theta = 0$ and 180 deg (see Fig. 3). For all average C_P plots in this paper, ranges of the axes were chosen for the best comparison between CFD solvers and the test data for that specific case. As such, the ranges can differ, and careful attention is required when comparing between cases. The averages for the solvers were nominally obtained by first washing out the numerical startup transient, then solving a sufficient amount of iterations to obtained a converged average or an average that does not change with more time steps. It was left to the individual users to produce the best average possible given the nature of the simulated

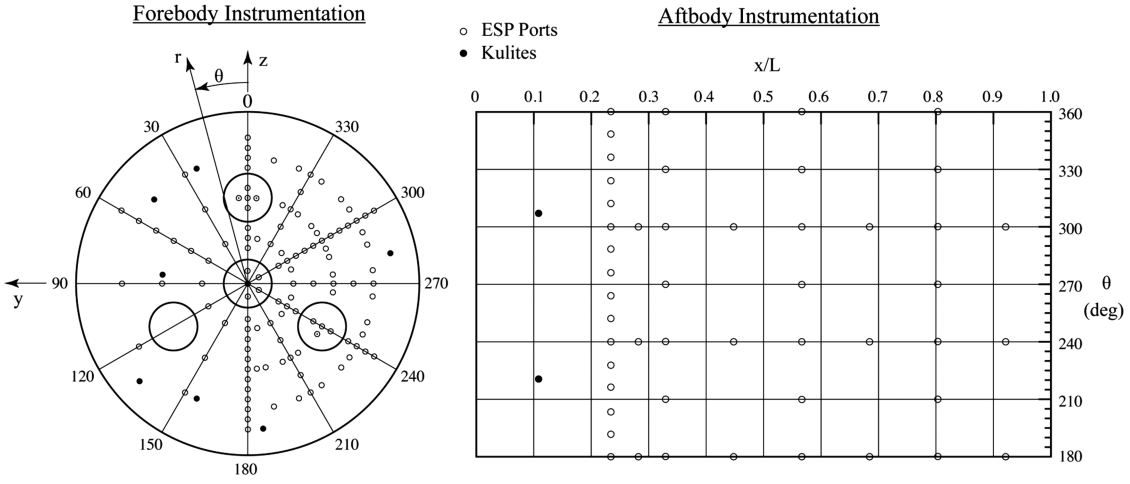

Fig. 3 Pressure-tap layout on test model face (left) and side body (right).

flow fields and limited computational resources. The flowfield images are instantaneous and include constructed Schlierens or shadowgraphs of the CFD solutions that were generated after the manner described in [22], and pressure coefficient on the model surface.

A. Sting Sensitivity

A concern of the test was the large sting used to mount the model in the tunnel. With a subsonic pocket behind the model, it was possible that influence from the sting could travel upstream and affect pressure measurements. To quantify these possible sting effects, cases with and without the sting were computed using OVERFLOW to make comparisons.

The geometry of the sting in the CFD computations is not an exact representation. The geometry was developed from photographs, with some dimensions supplied by the wind-tunnel staff. The sting also changed shape, in terms of both the location of the tubing as well as the shape of the casting, with every nozzle configuration change and roll angle increment. The present study is meant to be a first-order look into the effects of the sting and is not a comprehensive quantification of the sting effects for each model configuration of the test. Figure 4 shows images of the sting and the simplified CFD model.

Table 1 CFD run matrix

Run	Mach	Jets	C_T	α, deg	β, deg	ϕ, deg
106	1.8	1	4	0	0	180
116	2.4	1	4	0	0	180
223	2.4	1	4	0	0	0
223	2.4	1	4	0	−4	0
223	2.4	1	4	0	−8	0
223	2.4	1	4	0	−12	0
101	1.8	1	2	0	0	180
104	1.8	1	3	0	0	180
112	2.4	1	2	0	0	180
130	1.8	3	6	0	0	180
132	1.8	3	8	0	0	180
139	2.4	3	4	0	0	180
139	2.4	3	4	0	12	180
141	2.4	3	6	0	0	180
141	2.4	3	6	0	4	180
141	2.4	3	6	0	8	180
141	2.4	3	6	0	12	180
143	2.4	3	8	0	0	180
126	1.8	3	2	0	0	180
145	2.4	3	10	0	0	180
279	2.4	3	6	6	−10.33	30
309	2.4	3	6	−6	10.33	210
166	1.8	4	2	0	0	0
170	1.8	4	6	0	0	0
172	1.8	4	8	0	0	0
179	2.4	4	4	0	0	0
179	2.4	4	4	0	−4	0
179	2.4	4	4	0	−8	0
181	2.4	4	6	0	0	0
183	2.4	4	8	0	0	0
185	2.4	4	10	0	0	0

The condition simulated was the one-nozzle configuration, Mach 2.4, $Re/\text{ft} = 1.0$ million, $\alpha = \beta = 0$ deg. The cases were simulated with second-order time accuracy, and a running average of the surface pressure was computed. The unsteadiness of the run conditions did not allow the average surface pressure to completely converge or to not change with more time steps. This means unsteady effects were still a contributor to differences seen between the cases with and without the sting.

Figure 5 shows the average surface pressure along the model forebody (r/R) and side (x/L) from the sting-sensitivity study. The plots show that the case with the sting is closer to the test data on the model side in value and behavior. Deviation between the C_P values on the model face are due to small differences in predicting the shock structure behavior. Deviations aft of $x/L = 0.6$ are due to sting effects. Overall, it can be said that the sting effects were mainly confined to the aftmost pressure taps. Because of the computational expense, it was decided to forego the inclusion of the sting in the cases examined for this paper. It is understood that the pressure coefficient at the aft end of the model will most likely be underpredicted by the CFD.

B. Zero-Nozzle Configuration

The zero-nozzle configuration was the baseline, steady, supersonic blunt-body flow and was simpler than the jet-on cases. The CFD codes agreed well with each other, with test data from the LRC UPWT test, and at Mach 1.8 for the ARC UPWT, but deviation was noted at Mach 2.4 for the ARC UPWT data during testing. The model for the ARC UPWT test was located further aft in the test section than is common practice, and the Mach number deviation in the tunnel was not well characterized at that location. A second calibration run at the model nose location was performed, which provided corrections to the Mach 2.4 experimental data. After the corrections were applied, much better comparisons were reached. An example is run 50 from the ARC UPWT test, which was an overlap run to the LRC UPWT test and is seen in Fig. 6. The figure shows that all three CFD codes simulate the zero-nozzle configuration well.

C. One-Nozzle Configuration

SRP literature shows that different modes exist for the one-nozzle configuration depending on the jet-to-freestream pressure ratio [11,12]. At low pressure ratios, a long-jet penetration mode exists where the jet exhaust is unsteady and the bow shock has a large and fluctuating standoff distance from the model. At higher pressure ratios, the short-penetration mode exists where the flow is much

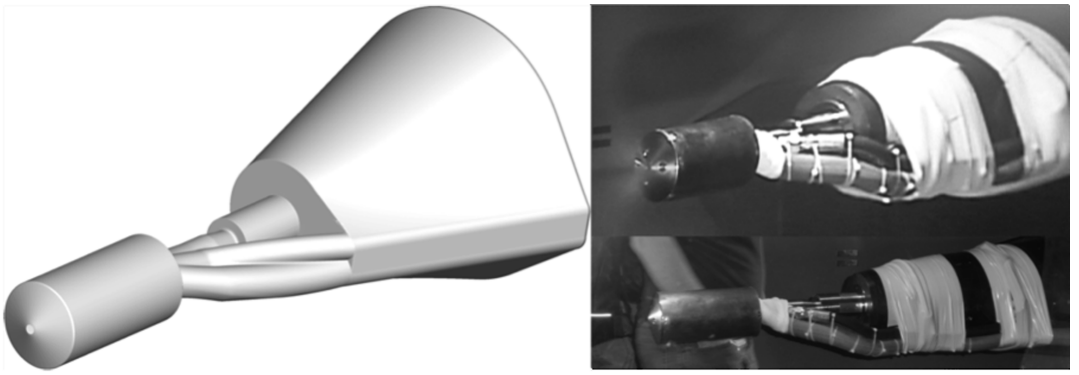

Fig. 4 Comparison of the OVERFLOW mesh representation (left) and the actual sting mounting apparatus used in the NASA ARC 9 × 7 ft UPWT (right).

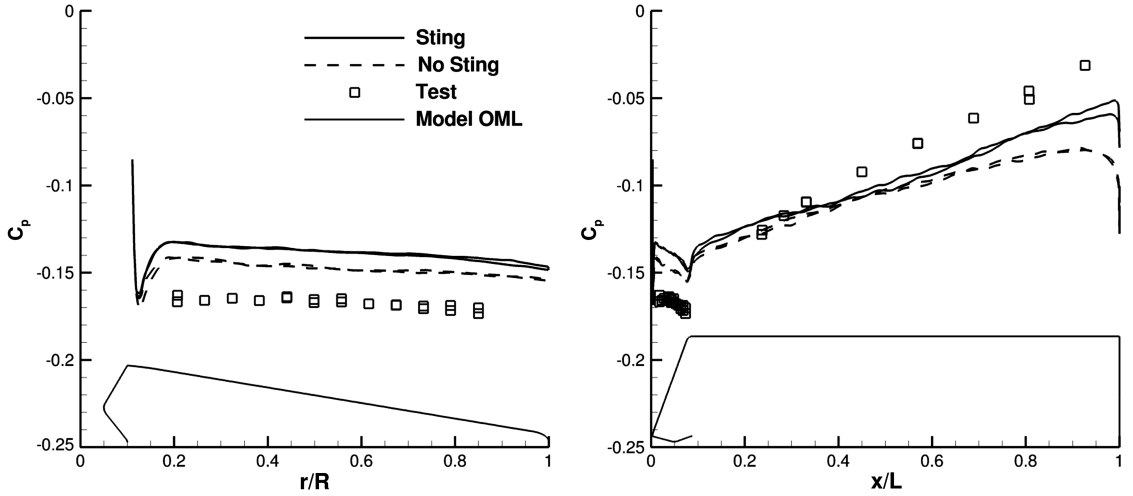

Fig. 5 Time-averaged C_P comparison between OVERFLOW results with and without the sting and wind-tunnel data along the model forebody (left) and side (right).

steadier and the bow shock has a significantly smaller standoff distance than in the long-jet penetration mode. It was observed in the LRC UPWT test that, once in the short-penetration mode, unsteadiness in the triple point (see [17] for explanation of the triple point) varied between a periodic oscillation and a smaller-scale aperiodic fluctuation. As angle of attack increased, the windward triple point oscillations became larger as the leeward triple point oscillations decreased. Then, for $\alpha = 20$ deg, the steadiness of the shock structure was lost as the plume and bow shock fluctuated chaotically. The CFD solvers did well simulating the one-nozzle cases of the LRC UPWT test in behavior and in matching the average surface pressure, with a trend that DPLR predicted a steadier flowfield than was seen in the test and FUN3D and OVERFLOW predicted the unsteady behavior seen in the test well. The different levels of predicted unsteadiness in the codes is attributed to turbulence modeling and grid resolution [16,17].

The highest C_T for the one-nozzle configuration in the ARC UPWT test was 4, where the limiting factor was the high-pressure

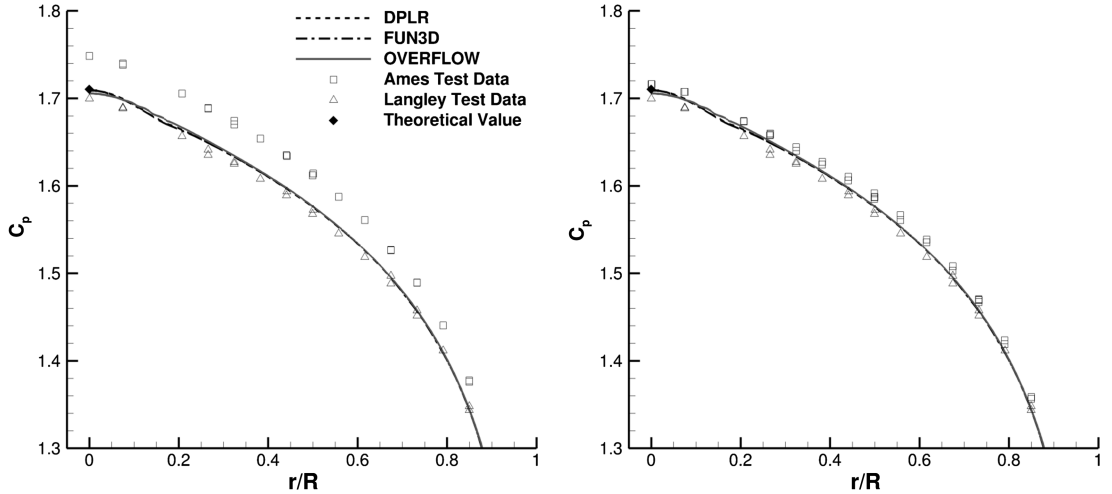

Fig. 6 Run 50 (Mach 2.4, zero-nozzle) from the ARC UPWT test compared to CFD and the LRC UPWT test before the wind-tunnel data Mach correction (left) and after (right).

system used for the jet flow. The CFD matrix focused on C_T of 4 with runs 106, 116, and 223 and how the behavior at that C_T varied with Mach number and β angle. Runs 101, 104, and 112 looked into lower thrust coefficients. All cases demonstrated the short-penetration mode.

Figure 7 visualizes the effect of C_T as seen in the test and how well the CFD matched that behavior. The increased size of the plume was simulated well with OVERFLOW, and average surface pressures matched well but were consistently underpredicted in the aft region of the model due to not modeling the sting. For run 104, the average C_P was overpredicted on the model forebody, caused by OVERFLOW predicting a periodic oscillation of the triple point. Shedding from the triple point propagated to the model forebody, which in turn affected the C_P on the surface. When the shedding is periodic instead of random, the energy is more organized, and the average C_P increases. Periodic shedding was not seen in the test for this run.

The effects of increasing β angle are shown in Fig. 8. As β angle increased, the windward triple point oscillation became more pronounced, and the leeward triple point became more stationary. This was predicted well by OVERFLOW, and the average surface C_P compared well on the model face with some underprediction on the model side. Run 223 $\beta = 12$ deg from the ARC UPWT test was similar in triple point behavior to run 165 $\alpha = 12$ deg from the LRC UPWT test [16,17].

Figure 9 combines the results from all codes and the test for run 223, $\beta = 0$ deg. All codes closely matched the shock structure seen

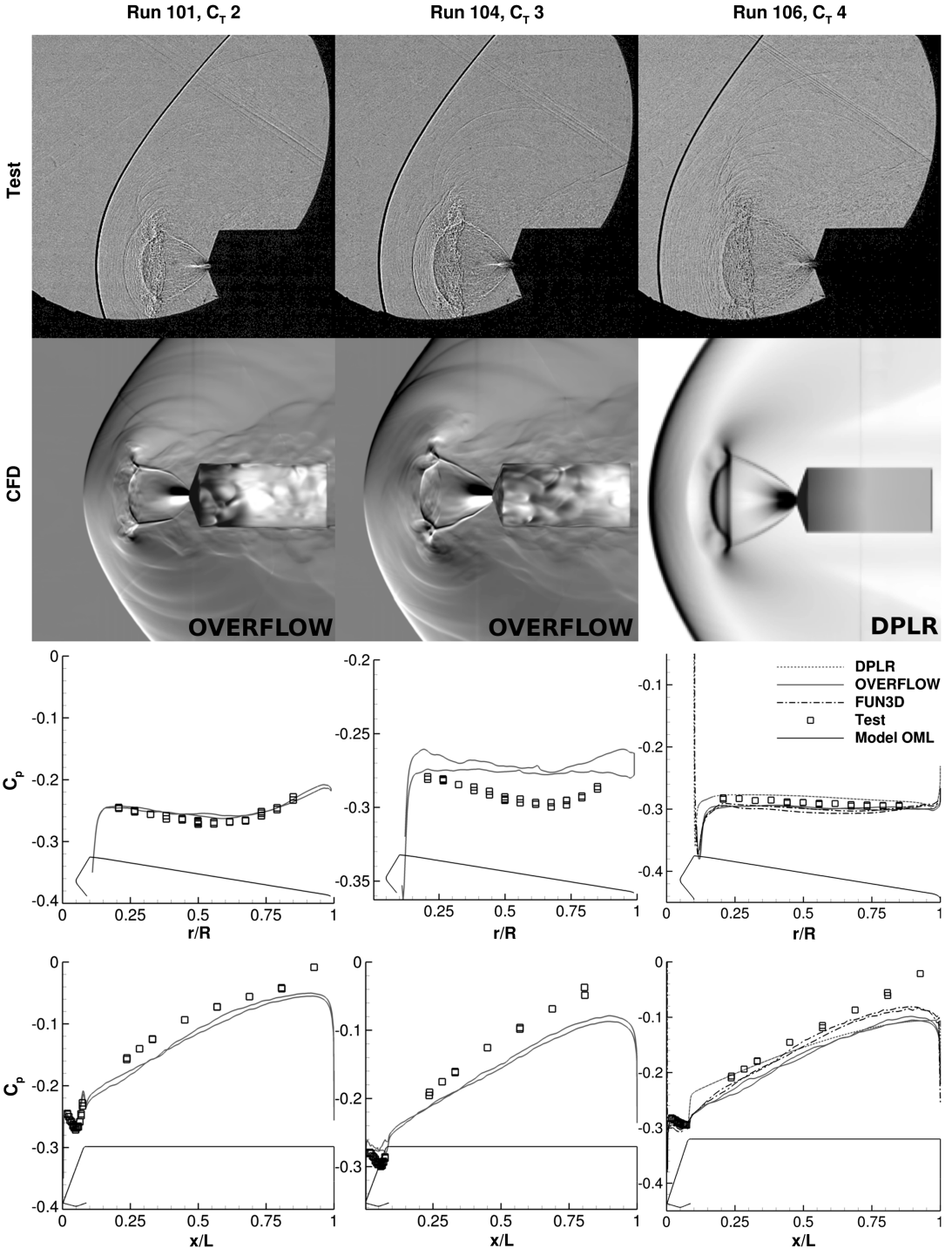

Fig. 7 Effects of C_T; test shadowgraph compared to CFD constructed Schlieren and time-averaged C_P comparison for the one-nozzle configuration at Mach 1.8.

in the test, including the standoff distances for the terminal shock, the contact surface, and the bow shock. The DPLR simulation reached a steady state, FUN3D predicted a periodic oscillation of the triple point, and OVERFLOW predicted the more random triple point oscillation seen in the test. On the model face, all codes overpredicted the average C_P near the shoulder, with FUN3D overpredicting the most due to simulating an organized shedding from the triple point. Along the model side, no significant differences were noted between the codes, and all underpredicted toward the aft end of the model due to not including the sting in the simulations.

Sample time traces of the aerodynamic contribution to axial force are seen in Fig. 10. Through the figure the level of unsteadiness of the codes is noted, with FUN3D and OVERFLOW similarly unsteady and DPLR more steady. For run 116, the unsteadiness is periodic. The dominant frequencies of the integrated axial force for the CFD codes are shown in Table 2.

Given the close comparisons in behavior and in average surface C_P, CFD fares well in simulating the one-nozzle configuration at these conditions. Some differences existed in the level of unsteadiness predicted by the solvers, which did not significantly affect differences in the average C_P. Two traits of the CFD that did affect the comparison to the tunnel data were sting effects and incorrectly predicting the triple point oscillation behavior.

D. Three-Nozzle Configuration

Observations from the LRC UPWT test [17] showed that for the three-nozzle configuration at thrust coefficients of 3, the jet-to-jet

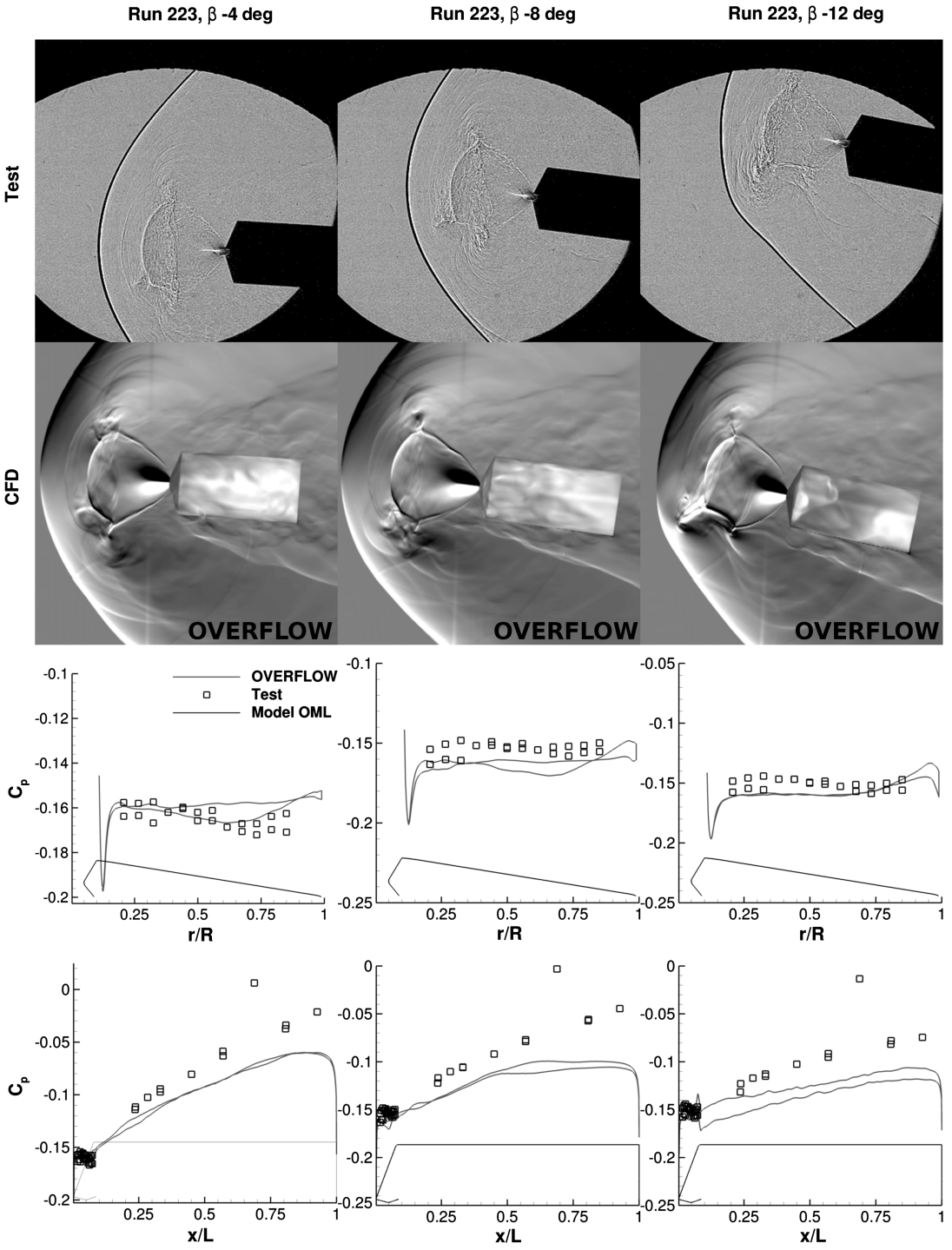

Fig. 8 Effects of β; test shadowgraph compared to CFD constructed Schlieren and time-averaged C_P comparison for the one-nozzle configuration, run 223: Mach 2.4, C_T 4.

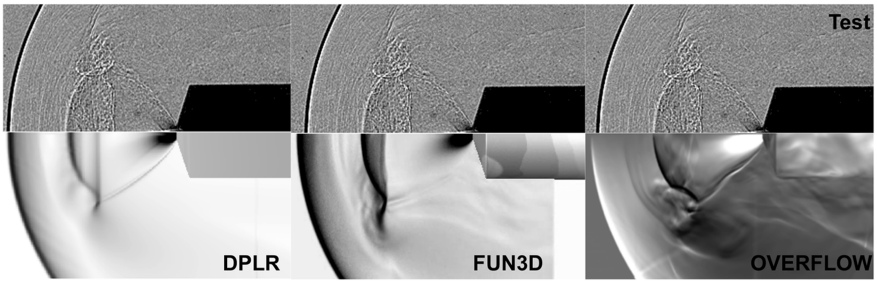

a) Shock structure comparisons

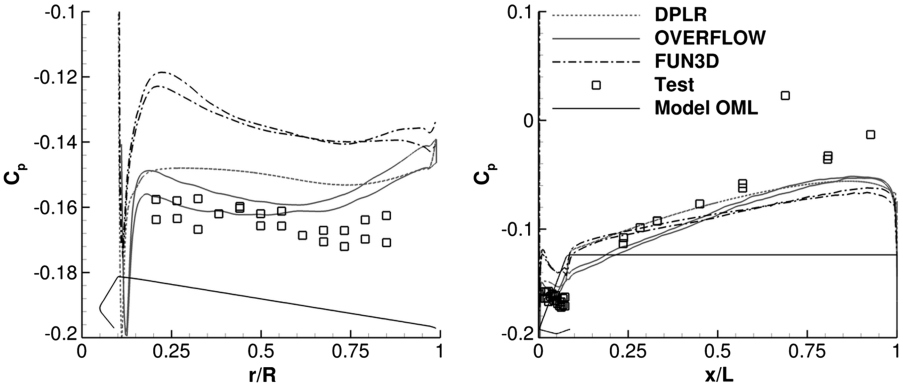

b) Average C_p comparisons

Fig. 9 Code-to-code and code-to-test comparison of run 223: one-nozzle, Mach 2.4, C_T 4, β 0 deg.

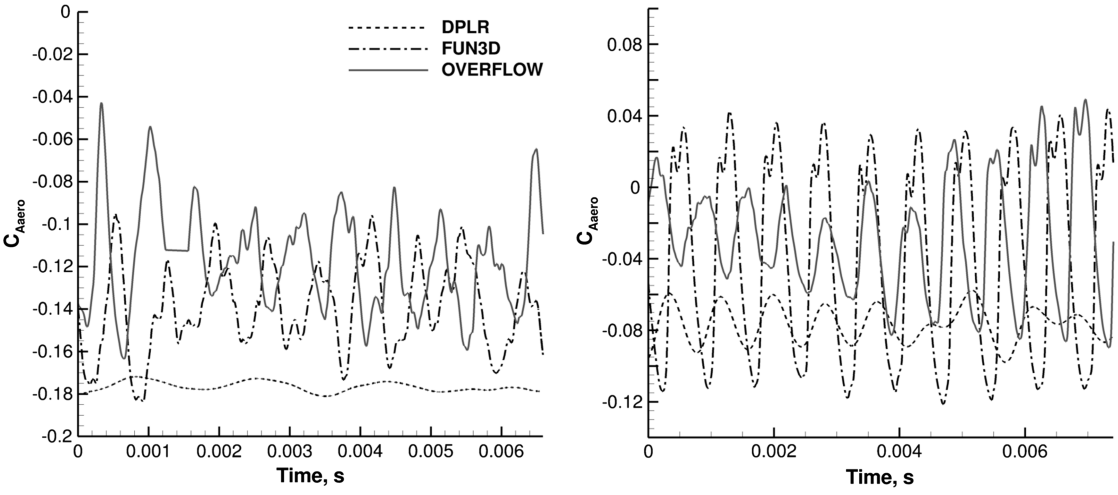

a) Run 106: Mach 1.8, C_T 4, β 0 deg

b) Run 116: Mach 2.4, C_T 4, β 0 deg

Fig. 10 Variation in time of the aerodynamic contribution to the axial force coefficient for a sample of one-nozzle cases.

interactions and bow shock behavior were aperiodically unsteady. The CFD did well in qualitative comparisons of the shock structure behavior, and varying success was obtained when comparing to the average surface pressure data. Discrepancies between the codes and test data at the model nose and shoulder implied a difference in how the codes were simulating the jet-to-jet interaction and the unsteady bow shock fluctuations, and how those impacted the pressure on the model face. A large discrepancy in data-acquisition rates did exist between the CFD and the WTT. Rates were on the order of 10 Hz for the WTT and 10 kHz for the CFD simulations. An entire CFD run could fit within the time between two pressure-tap readings, meaning high-frequency fluctuations captured by the CFD codes were not captured by the WTT data system, and low-frequency fluctuations captured by the WTT data system were not captured by the CFD. This introduced an error source that increased when unsteady frequencies became very high or very low. A run at zero angle of attack and C_T of six showed that the plumes and bow shock became nearly steady.

Table 2 Dominant frequencies (in kilohertz) from CFD for one-nozzle cases

Solver	Run 106	Run 116
DPLR	0.60	0.67
FUN3D	1.38	1.34
OVERFLOW	1.42	1.34

The higher thrust coefficients tested in the ARC UPWT demonstrated steadier flow than the lower thrust coefficients seen in the LRC UPWT test. This trend is shown in Fig. 11, where run 126 was more unsteady at a C_T of 2 than runs 130 and 132, which were at C_T of 6 and 8, respectively. The OVERFLOW results for run 126 differed in

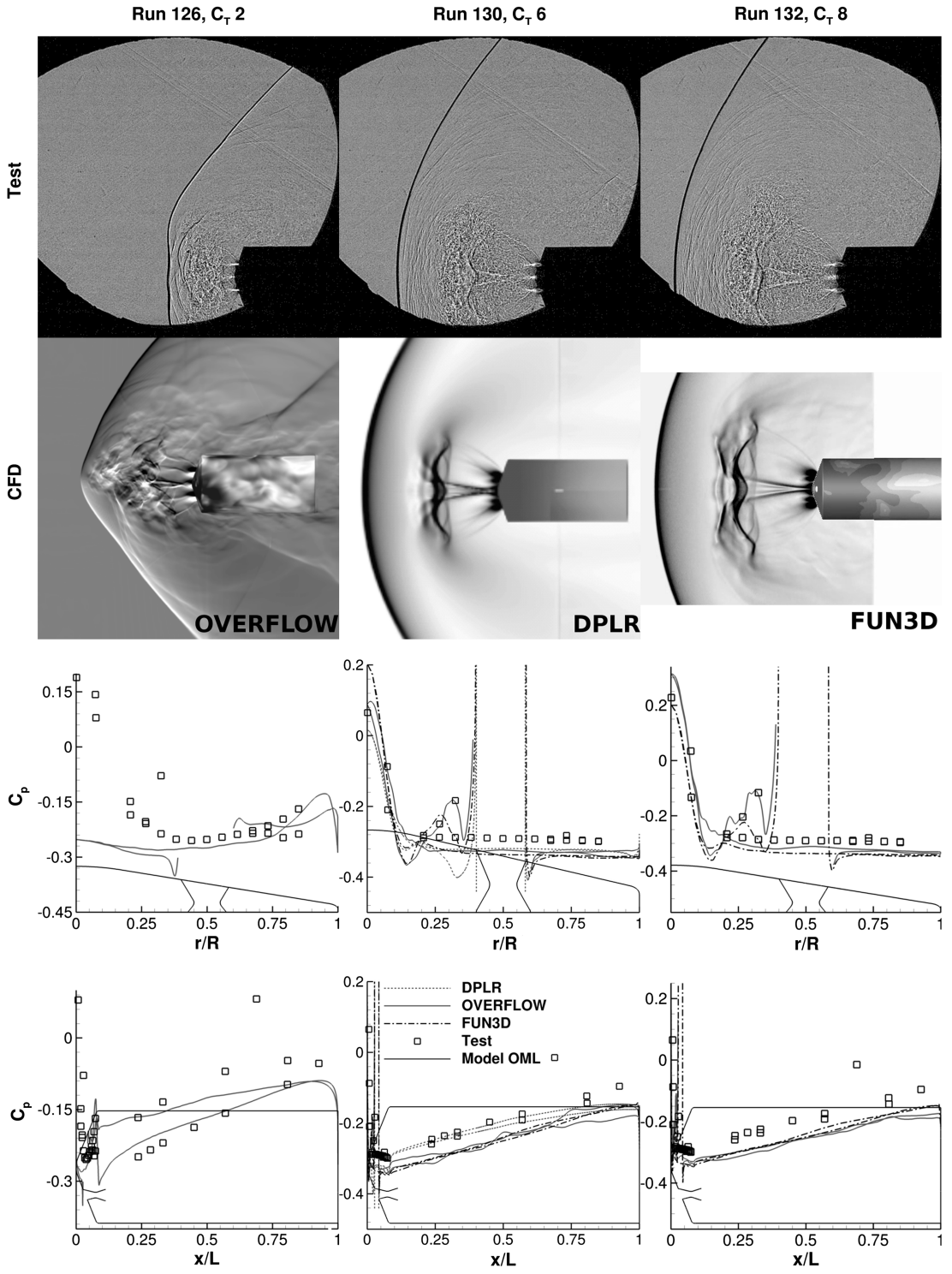

Fig. 11 Effects of C_T; test shadowgraph compared to CFD constructed Schlieren/shadowgraph and time-averaged C_P comparison for the three-nozzle configuration at Mach 1.8.

behavior and in average surface C_P from the test, especially at the model nose. As C_T increased, the steadiness did as well, as did the agreement with the CFD simulations. Good agreement was seen between the codes, with the largest differences at the model nose and near the nozzle exit. The CFD underpredicted the C_P for the majority of the model face and side, with overpredictions at the nose by FUN3D for run 130 and by OVERFLOW for run 132. OVERFLOW closely matched the test average C_P at the nose for run 130 and near the nozzle for runs 130 and 132. DPLR, which reached a steady-state solution, closely matched the average C_P on the model side for run 130.

As β increased (see Fig. 12), the test showed the shock structure maintaining its basic shape, with a noticeable difference in the windward triple point of the windward plume, which increased in oscillation amplitude. This same behavior existed for all tested β angles up to 12 deg. Here lies a weakness in the OVERFLOW results. For β angles up to 8 deg, the windward plume maintained its shape, but for $\beta = 12$ deg, the windward plume was compressed, and the resulting flow structure was more unsteady than what was seen in the test. The difference in flow behavior, however, did not greatly influence the average surface pressure comparison; all cases still compared well to the test data.

The effects of roll ϕ at high angle of attack is shown in Fig. 13. In the test, the three plumes still maintained their shapes regardless of roll, but in the OVERFLOW results, only $\phi = 210$ deg showed that

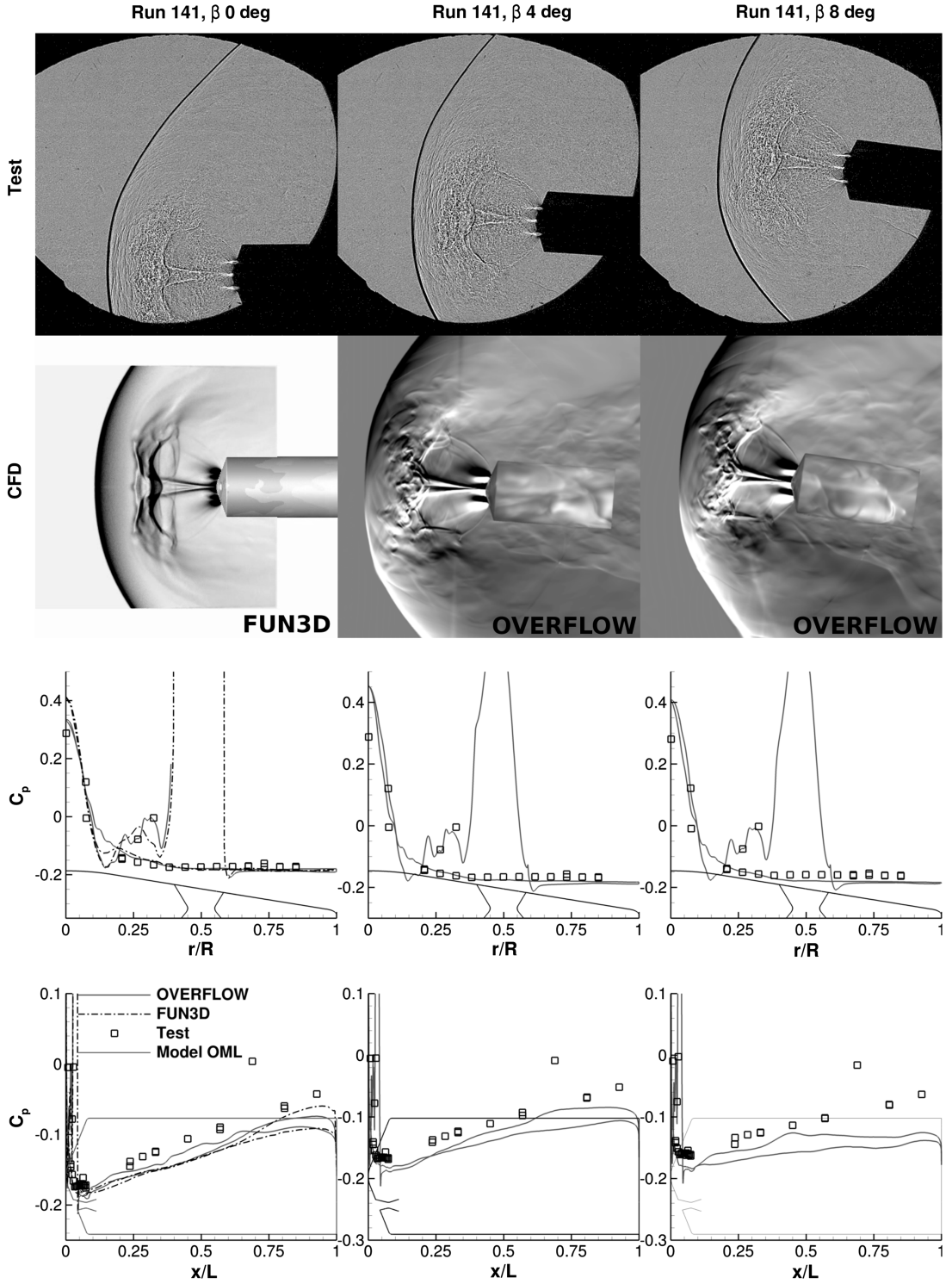

Fig. 12 Effects of β; test shadowgraph compared to CFD constructed Schlieren/shadowgraph and average surface pressure comparison for the three-nozzle configuration, run 141: Mach 2.4, C_T 6.

behavior where the other roll angles showed a compressed windward plume. For the cases with $\phi = 180$ and 30 deg, the compressed plume was more directly in line with the oncoming tunnel flow, or more relatively windward than for the $\phi = 210$ deg case. For the $\phi = 210$ deg case, the two windward plumes were equally windward, and neither was as directly in line with the flow as the other ϕ cases.

The high pressure at the nose of the model for the three-nozzle configuration should not be taken to be resultant of oncoming freestream flow penetrating the space between the plumes. Instead, the high-pressure region is caused by a recirculation zone created by entrapment of jet exhaust and entrainment from surrounding flow. Figure 14 shows the velocity vector field near the model nose to visualize the recirculation zone for run 145: three-nozzle, Mach 2.4, $C_T = 10$. The vectors are on the symmetry plane and are from an OVERFLOW solution. Differences in surface C_P between the codes for the three-nozzle configuration can be attributed to differences in modeling the recirculation caused by that entrainment and entrapment.

Run 139 was used for a code-to-code comparison and is visualized in Fig. 15. In the test, the flow was more unsteady than shown in the CFD solutions. FUN3D was closest to the unsteady behavior but

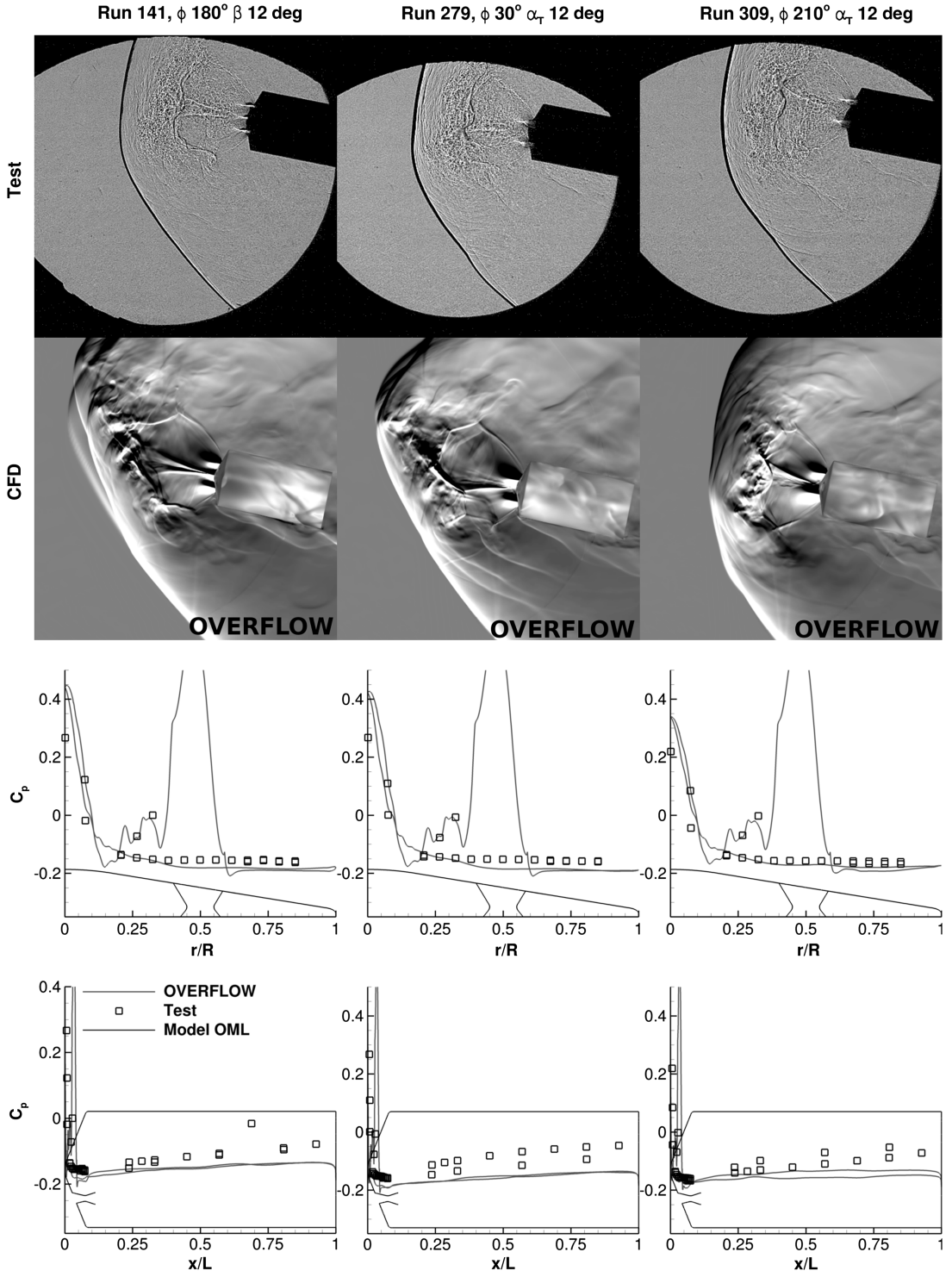

Fig. 13 Effects of ϕ; test shadowgraph compared to CFD constructed Schlieren and average surface pressure comparison for the three-nozzle configuration at Mach 2.4, C_T 6.

eventually reached a steady state. This demonstrated that the boundaries between different modes of behavior for SRP (in this case, the boundary between unsteady and much steadier flow as C_T increases) was not captured well by the CFD codes. Any variation between WTT conditions and simulated conditions, such as test section flow nonuniformity, can contribute to the differences noted in behavioral mode transitions between the solvers and the test. For the average C_P, FUN3D overpredicted at the nose and bounded the test data on the model side, DPLR closely matched on the face and side with an underprediction near the nozzle exit, and OVERFLOW closely matched on the face but predicted nearly symmetric C_P on the side.

Time traces of the aerodynamic contribution to axial force for runs 130 and 143 are seen in Fig. 16. The plot shows the steady state reached by DPLR for run 130 and similar unsteady behavior between FUN3D and OVERFLOW, with OVERFLOW predicting a lower magnitude of force. Dominant frequencies were difficult to obtain for all CFD solvers for these cases due to the many frequencies present.

Confidence in the ability of CFD to simulate three-nozzle SRP configurations is stronger for higher C_Ts ($\gtrsim$4) than for lower C_Ts ($\lesssim$4). The boundary between the unsteady lower C_T and the much steadier higher C_T is not well predicted by CFD, but once the steadier mode is obtained, better agreement between the CFD solvers and the test data is achieved. The LRC UPWT CFD validation exercise

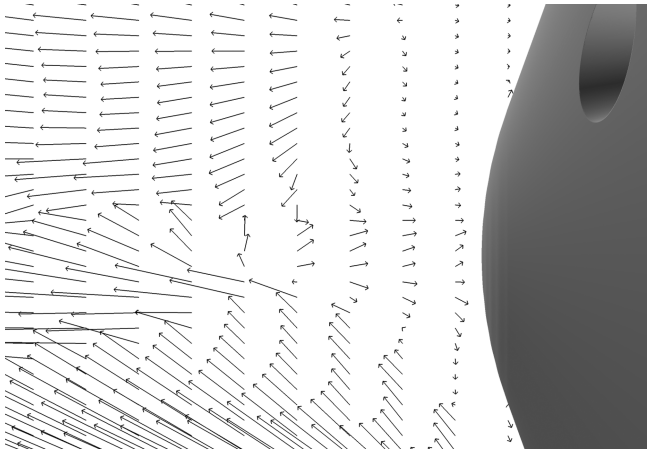

Fig. 14 Velocity vector visualization of the three-nozzle configuration recirculation zone near the model nose.

showed that all solvers closely matched the wind-tunnel test qualitatively in behavior, but differences in average surface C_P did exist. A possible reason for the deviation between the solvers and the test for low C_Ts is that the solver best practices were established for one-nozzle SRP flow but may not be optimal for multinozzle flows with interacting shear layers.

E. Four-Nozzle Configuration

For the four-nozzle configuration, the LRC UPWT test showed a short-penetration jet structure behavior at zero angle of attack. A discrepancy between the CFD codes for this behavior was noted. Runs 307 and 311 were the same in Mach number (4.6) and thrust coefficient (2) but differed in a roll angle of 0 and 180 deg, respectively. The test showed the same short-penetration jet behavior for both runs, but DPLR showed a larger shock standoff distance for run 307, and OVERFLOW showed a larger and fluctuating shock standoff distance for run 311. This implied a difference in modes for the four-nozzle configuration, and the boundary between the modes was not well defined by the CFD codes.

In the ARC UPWT test at lower C_T, the flow was steadier with a shorter bow shock standoff distance similar to the LRC UPWT test, but at higher C_T, the flow became chaotic with large and oscillating shock standoff distances. The CFD matched the behavior of the zero β cases well, but not much value was placed in the average surface pressure comparisons. Because the flow was chaotic and the data-acquisition rates varied so greatly between the CFD and WTT data, the averages obtained by the CFD and WTT differed greatly. The WTT data-acquisition rates were also not sufficient to gather enough samples for this high-frequency chaotic flow.

In the LRC UPWT test, it was shown that, for a roll angle of 0 deg, unsteadiness increased with angle of attack. For a roll angle of 180 deg, an angle of attack of 12 deg was unsteady, while an angle of attack of 20 deg settled into a steadier mode. All of these behaviors were simulated well with the CFD solvers, with the exception at an angle of attack of 0 deg, already discussed. The average surface pressures for the LRC UPWT test compared well between the codes for all cases, with the largest discrepancies found at the model shoulder. Similar to the three-nozzle configuration, the differences in average C_P at the shoulder implies differences in simulated shock fluctuations that impacted the model face.

As β angle increased in the ARC UPWT test, the level of unsteadiness decreased, as seen with run 179 in Fig. 17. This behavior was not matched by OVERFLOW, which continued to predict a highly chaotic flowfield at β angles of 4 and 8 deg. This may be a limitation of the grid system and numerical models used, which were optimized for a one-nozzle configuration and then applied to multinozzle configurations.

Code-to-code comparisons can be seen in Fig. 18 for run 166 (Mach 1.8, $C_T = 4$). The test still demonstrated the steadier, shorter shock standoff distance at lower thrust coefficients. This behavior was matched by FUN3D and OVERFLOW, but a larger standoff distance was predicted by DPLR. The average surface C_P from DPLR overpredicted FUN3D and OVERFLOW, both of which were closer to the test data. The FUN3D C_P data showed a more dynamic behavior than OVERFLOW and DPLR, a result of insufficient

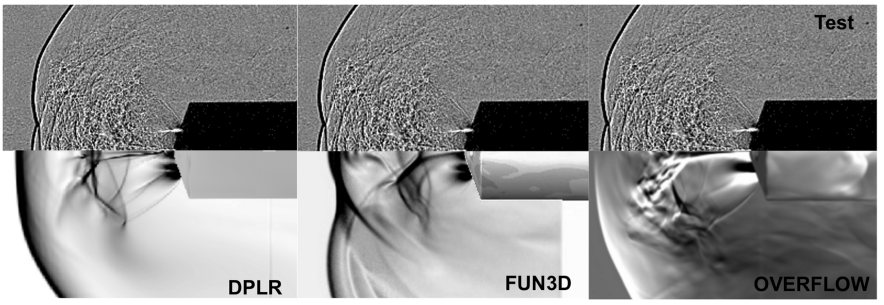

a) Shock structure comparisons

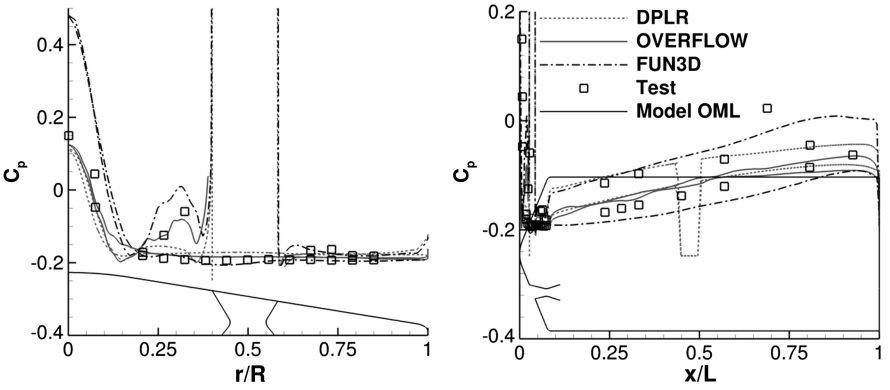

b) Average C_p comparisons

Fig. 15 Code-to-code and code-to-test comparison of run 139: three-nozzle, Mach 2.4, C_T 4.

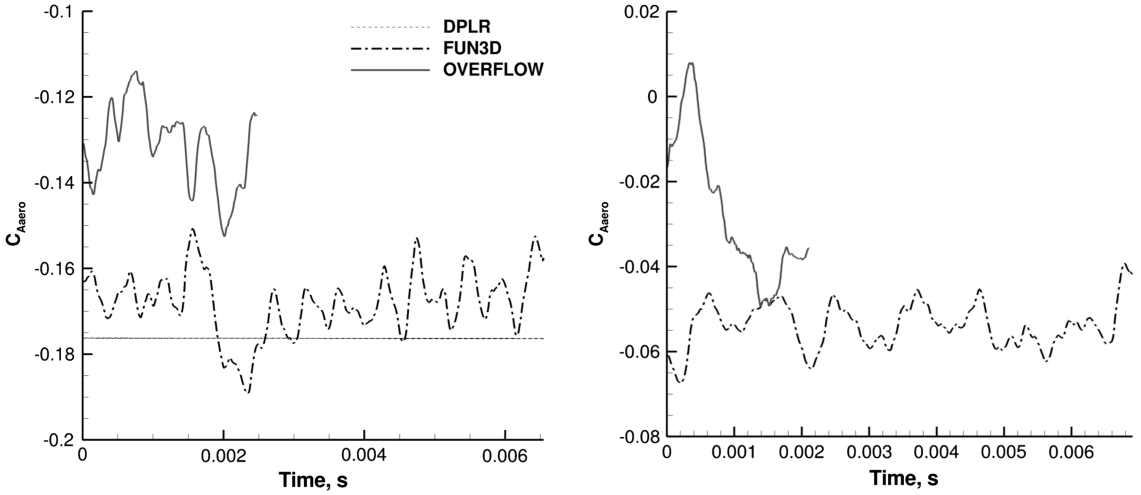

a) Run 130: Mach 1.8, C_T 6, β 0 deg b) Run 143: Mach 2.4, C_T 8, β 0 deg

Fig. 16 Variation in time of the aerodynamic contribution to the axial force coefficient for a sample of three-nozzle cases.

averaging for this case. A comparison of the aerodynamic contribution to the total axial force is seen in Fig. 19 for runs 172 and 179. All CFD solvers predicted unsteadiness, with FUN3D and OVERFLOW predicting aperiodic unsteadiness for runs 172 and 179 and DPLR predicting periodic unsteadiness for run 179.

The confidence in the ability of the CFD solvers to simulate four-nozzle flow is not as strong as it is for the one-nozzle configuration. The change in the short-penetration shock standoff distance to the wildly chaotic behavior was predicted to be at different points between the CFD solvers. Because of the highly unsteady behavior of the four-nozzle configuration at C_T greater than 4, it was difficult to obtain reasonable average surface pressure comparisons between the CFD and the WTT data. Also, steadier modes at angle of attack were seen for the four-nozzle configuration that were not simulated with the CFD.

F. Thrust Dominance

For the SRP cases discussed, the total axial force was dominated by the thrust coefficient and the contribution of the aerodynamic axial force was small. This can be seen in the bar chart in Fig. 20, where the gray section of the bars represent C_T, and the black sections represent $C_{A,\text{aero}}$. This raises the question to whether aerodynamic effects are negligible for these types of SRP flows. More research needs to be conducted to answer this question. Entry trajectories and vehicle attitudes as well as spacecraft scale need to be taken into consideration. A high-frequency oscillation at the WTT scale will be a much lower frequency at the flight scale and may have more contribution to vehicle stability. Normal force and vehicle moments also need to be taken into consideration, especially for nonzero vehicle entry attitudes.

G. Computational Cost

Table 3 shows a breakdown of the computational cost for each of the codes for a typical SRP run. This is not a perfect comparison because the numbers represented are either just from a single run or averages of multiple runs. All cases were computed on the Pleiades NASA Advanced Supercomputing cluster, an SGI Ice cluster, on either Nehalem or Westmere nodes. Because each code used different amounts of time, number of iterations, number of subiterations, and number of grid points, a common metric of CPU seconds per iteration per grid point between the codes is reported for comparison.

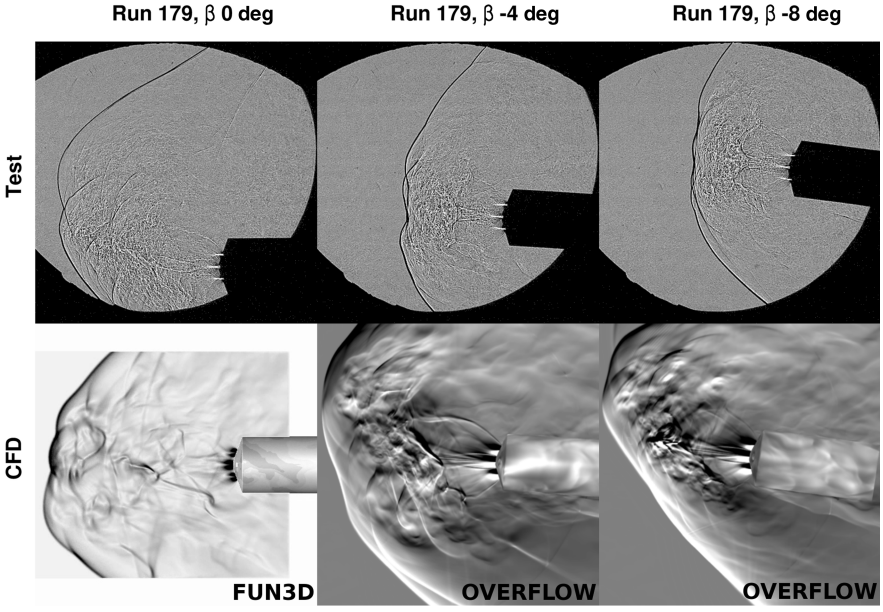

Fig. 17 Effects of β; test shadowgraph compared to CFD constructed Schlieren/shadowgraph and average surface pressure comparison for the four-nozzle configuration, run 179: Mach 2.4, C_T 4.

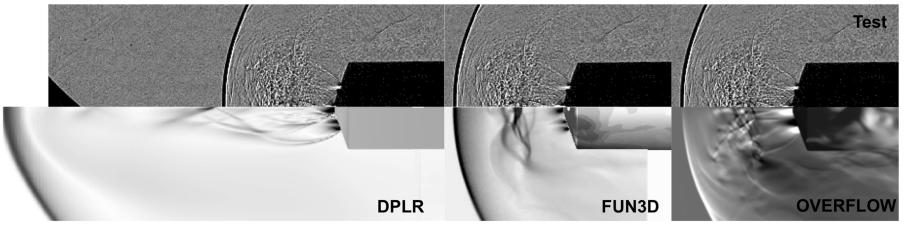

a) Shock structure comparisons

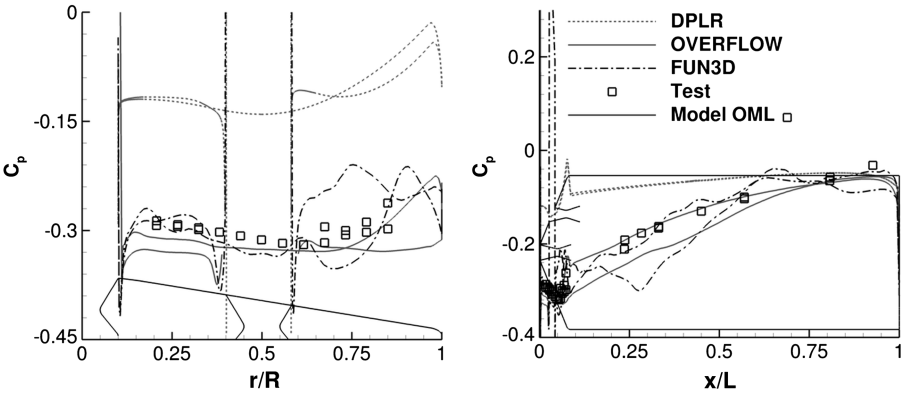

b) Average C_P comparisons

Fig. 18 Code-to-code and code-to-test comparison of run 166: four-nozzle, Mach 1.8, C_T 4.

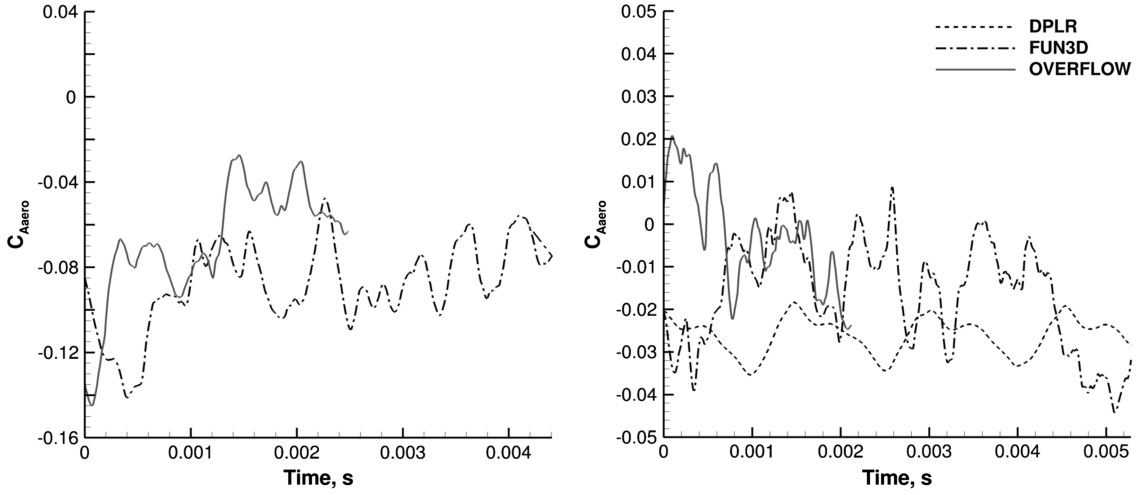

a) Run 172: Mach 1.8, C_T 8, β 0 deg b) Run 179: Mach 2.4, C_T 4, β 0 deg

Fig. 19 Variation in time of the aerodynamic contribution to the axial force coefficient for a sample of four-nozzle cases.

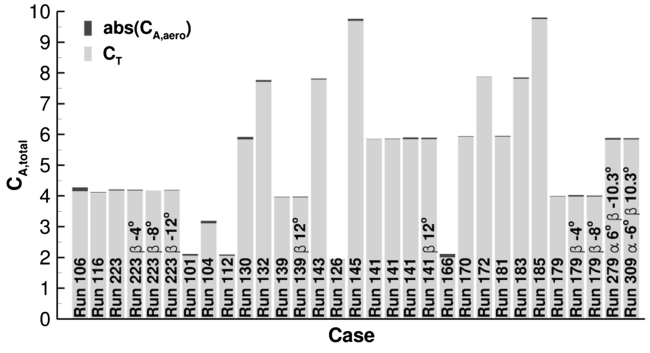

Fig. 20 Comparison of the contributions of thrust and aerodynamics to the total axial force for the ARC UPWT CFD cases run by OVERFLOW.

Part of the requirement for these validation runs was to test the ability of the solvers to predict SRP flowfields. For this reason, time-accurate runs were necessary because it is impossible to know beforehand if the unsteady effects played a large role in the aerodynamic effects. Costs for validation cases were large; however, for production runs of parametric studies or database generation, the computational costs should be able to drop significantly as either steady-state runs or faster numerical and time step processes are adopted.

Table 3 Computational cost per case

Solver	CPU hours	Iterations	Grid points	CPU seconds per iteration per grid point
FUN3D	28,000	39,500	4.2e7	6.1e-05
DPLR	44,500	106,000	5.3e7	2.9e-05
OVERFLOW	35,039	73,500	8.5e7	2.0e-05

IV. Conclusions

A second wind-tunnel test for validation of computational fluid dynamics in supersonic retropropulsion conditions was conducted in the Ames Unitary 9×7 ft tunnel. The Ames test had a larger test section than the previous test, which took place in the Langley Unitary 4×4 ft tunnel. With the larger test section, higher thrust coefficients were obtained that more closely match flight requirements. The three solvers used were DPLR, FUN3D, and OVERFLOW.

For the one-nozzle configuration, little difference was observed between the higher thrust coefficients of 4 obtained in the Ames test and the lower thrust coefficients of 2 obtained in the Langley test. The short-penetration shock interaction structure was observed, and oscillations at the triple point increased for the windward triple point as angle of attack was increased. The solvers compared well to the one-nozzle test data, only varying in predicting periodic oscillations of the triple point when random oscillations were observed in the test. Average surface pressure comparisons were promising, building confidence in the ability of the solvers to predict one-nozzle configuration supersonic retropropulsion.

For the three-nozzle configuration, the unsteady behavior noted at lower thrust coefficients of 2 did not exist for higher thrust coefficients where the flow structure becomes more steady, especially in the bow shock. This behavior was predicted well with the solvers, and average surface pressures agreed well with the test data. The area of greatest deviation between the codes was along the model shoulder and at the model nose. The differences at the nose are attributed to differences in entrainment, entrapment, and recirculation being simulated between the codes at the model nose as well as any shear-layer interaction that may be occurring between the plumes. At β and α_T of 12 deg, OVERFLOW did not predict the same behavior as the test, predicting a more compressed windward plume for most cases. This discrepancy in qualitative comparison did not seem to greatly influence the average surface pressure comparison.

For the four-nozzle configuration, a steadier mode with a short shock standoff distance existed for lower thrust. As thrust was increased, the flow became highly unsteady with the bow shock standoff distance aperiodically oscillating between small and large standoff distances. The unsteady flowfield was predicted well with the codes, but the average surface pressures were not comparable to test data, presumably due to large differences in data-acquisition rates between the solvers and the test and the large difference in time-averaging windows. At $\beta = 4$ and 8 deg, a steadier mode was noted that was not predicted by OVERFLOW, which continued to predict a largely chaotic flowfield.

The validation study built confidence in the ability of the solvers to simulate one-nozzle configurations at all β angles tested and high-thrust three-nozzle configurations at $\beta \leq 8$ deg. The ability to simulate the behavior seen in the high-thrust four-nozzle cases was also demonstrated, but average surface pressure comparisons were poor. The ability of the solvers to predict the exact boundary between steady and unsteady modes for one-, three-, and four-nozzle configurations was not demonstrated, and in fact offered contradictory results in both the Langley and Ames tests for the four-nozzle $\alpha/\beta = 0$ deg configuration. The average surface pressure comparisons were the best for the one-nozzle configuration and for the steadier runs of the three- and four-nozzle configurations. This correlates to steadier flowfields where the large difference in data-acquisition rates between the solvers and the test did not greatly influence the averages obtained. Another possible error source may be the grid systems and numerical models used for the codes, which were optimized for one-nozzle supersonic retropropulsion flow, not for multinozzle flows with shear-layer interactions.

Thrust dominance and computational costs were also mentioned. Computational costs were high for validation but could be much less for production.

Future work for computational-fluid-dynamics validation would include hot-fire rocket tests including startup transients, more flight-relevant calculations including Mars atmospheric and rocket exhaust gases, and an application to flight-scaled spacecraft to better understand the influence of aerodynamics on stability and control. Future wind-tunnel tests could include pressure measurement instrumentation along the model shoulder to help validate the solvers in that area. More research for the solvers may be needed to properly define the boundaries between different behavioral modes as well as an optimization of a grid system for multinozzle SRP flowfields.

Acknowledgments

Pieter G. Buning of NASA Langley Research Center, Hampton, Virginia, and Phillip C. Stuart, Thomas M. Booth, and Darby J. Vicker of NASA Johnson Space Center, Houston, Texas provided valuable guidance on gridding and solver best practices for OVERFLOW. William T. Jones of NASA Langley Research Center, Hampton, Virginia, provided the GridEx/batchEx unstructured grid-generation framework and helped with its application to generate FUN3D grids. Todd R. White and Andrew J. Hyatt of ERC Inc., Moffett Field, California, helped develop DPLR best practices and provided overset gridding assistance for DPLR cases. David A. Saunders of ERC Inc., Moffett Field, California, developed the code used for OVERFLOW and DPLR simulated Schlieren/shadowgraph visualizations. The authors would like to acknowledge the support of the Exploration Technology Development and Demonstration (ETDD) Program, which was managed at NASA Glenn Research Center. The work documented herein was performed as part of ETDD's Entry, Descent, and Landing Technology Development Project, which was managed at NASA Langley Research Center and supported by NASA Ames Research Center, NASA Johnson Space Center, and the Jet Propulsion Laboratory.

References

[1] Braun, R. D., and Manning, R. M., "Mars Exploration Entry, Descent, and Landing Challenges," *Journal of Spacecraft and Rockets*, Vol. 44, No. 2, 2007, pp. 310–323. doi:10.2514/1.25116

[2] Steinfeldt, B. A., Theisinger, J. E., Korzun, A. M., Clark, I. G., Grant, M. J., and Braun, R. T., "High Mass Mars Entry, Descent, and Landing Architecture Assessment," *AIAA SPACE 2009 Conference & Exposition*, AIAA Paper 2009-6684, Sept. 2009.

[3] Zang, T. A., Dwyer–Dianciolo, A. M., Kinney, D. J., Howard, A. R., Chen, G. T., Ivanov, M. C., Sostaric, R. R., and Westhelle, C. H., "Overview of the NASA Entry, Descent and Landing Systems Analysis Study," *AIAA SPACE 2010 Conference & Exposition*, AIAA Paper 2010-8649, Aug. 2010.

[4] Edquist, K. T., Dyakonov, A. A., Korzun, A. M., Shidner, J. D., Studak, J. W., Tigges, M. A., Kipp, D. M., Prakash, R., Trumble, K. A., and Dupzyk, I. C., "Development of Supersonic Retro-Propulsion for Future Mars Entry, Descent, and Landing Systems," (to be published).

[5] Korzun, A. M., and Braun, R. D., "Performance Characterization of Supersonic Retropropulsion Technology for High-Mass Mars Entry Systems," *Journal of Spacecraft and Rockets*, Vol. 47, No. 5, 2010, pp. 836–848. doi:10.2514/1.49803

[6] Korzun, A. M., Braun, R. D., and Cruz, J. R., "Survey of Supersonic Retropropulsion Technology for Mars Entry, Descent, and Landing," *Journal of Spacecraft and Rockets*, Vol. 46, No. 5, 2009, pp. 929–937. doi:10.2514/1.41161

[7] Wright, M. W., White, T., and Mangini, N., "Data Parallel Line Relaxation (DPLR) Code User Manual Acadia Version 4.01.1," NASA TM-2009-215388, Oct. 2009.

[8] Anderson, W. K., and Bonhaus, D. L., "An Implicit Upwind Algorithm for Computing Turbulent Flows on Unstructured Grids," *Computers and Fluids*, Vol. 23, No. 1, 1994, pp. 1–21. doi:10.1016/0045-7930(94)90023-X

[9] Anderson, W. K., Rausch, R. D., and Bonhaus, D. L., "Implicit/Multigrid Algorithm for Incompressible Turbulent Flows on Unstructured Grids," *Journal of Computational Physics*, Vol. 128, No. 2, 1996, pp. 391–408. doi:10.1006/jcph.1996.0219

[10] Nichols, R., and Buning, P., *User's Manual for OVERFLOW 2.1t*, University of Alabama, Birmingham, AL, Aug. 2008.

[11] Jarvinen, P. O., and Adams, R. H., "The Aerodynamic Characteristics of Large Angled Cones with Retrorockets," NASA CR-NAS7-576, Feb. 1970.

[12] Daso, E. O., Pritchett, V. E., Wang, T. S., Ota, D. K., Blankson, I. M., and Auslender, A. H., "Dynamics of Shock Dispersion and Interactions in Supersonic Freestreams with Counterflowing Jets," *AIAA Journal*, Vol. 47, No. 6, 2009, pp. 1313–1326. doi:10.2514/1.30084

[13] Trumble, K. A., Schauerhamer, D. G., Kleb, W. L., Carlson, J. R., Buning, P. G., Edquist, K. T., and Barnhardt, M. D., "An Initial Assessment of Navier–Stokes Codes Applied to Supersonic Retro–Propulsion," *10th AIAA/ASME Joint Thermophysics and Heat Transfer Conference*, AIAA Paper 2010-5047, June 2010.

[14] Berry, S. A., Laws, C. T., Kleb, W. L., Rhode, M. N., Spells, C., Mccrea, A. C., Trumble, K. A., Schauerhamer, D. G., and Oberkampf, W. L., "Design and Analysis of a Supersonic Retropropulsion Validation Experiment in the NASA Langley Unitary Plan Wind Tunnel Test," (to be published).

[15] Trumble, K. A., Schauerhamer, D. G., Kleb, W. L., Carlson, J. R., and Edquist, K. T., "Analysis of Navier–Stokes Codes Applied to Supersonic Retro-Propulsion Wind Tunnel Test," (to be published).

[16] Kleb, W. L., Schauerhamer, D. G., Trumble, K. A., Sozer, E., Barnhardt, M. D., Carlson, J. R., and Edquist, K. T., "Toward Supersonic Retropropulsion CFD Validation," (to be published).

[17] Schauerhamer, D. G., Trumble, K. A., Kleb, W. L., Carlson, J. R., and Edquist, K. T., "Supersonic Retropropulsion Computational Fluid Dynamics Validation with Ames 9'x7' Test Data," (to be published).

[18] Codoni, J. R., and Berry, S. A., "Analysis of Dynamic Data form Supersonic Retropropulsions Experiments in NASA Lengley's Unitary Plan Wind Tunnel," (to be published).

[19] Berry, S. A., Rhode, M. N., and Edquist, K. T., "Supersonic Retropropulsion Experimental Results from the NASA Ames 9- x 7-Foot Supersonic Wind Tunnel," (to be published).

[20] Rhode, M. N., and Oberkampf, W. L., "Estimation of Uncertainties for Supersonic Retropropulsion Model Validation Experiment in a Wind Tunnel," (to be published).

[21] Aeschliman, D. P., and Oberkampf, W. L., "Experimental Methodology for Computational Fluid Dynamics Code Validation," *AIAA Journal*, Vol. 36, No. 5, 1998, pp. 733–741. doi:10.2514/2.461

[22] Yates, L. A., "Interferograms, Schlieren, and Shadowgraphs Constructed from Real- and Ideal-Gas, Two- and Three-Dimensional Computed Flowfields," NASA CR-190054, Jan. 1992.

C. Chang
Associate Editor